Contents lists available at Science-Gate

International Journal of Advanced and Applied Sciences

Journal homepage: http://www.science-gate.com/IJAAS.html

Fabrication and characterization of nanostructured Fe–28Mn–6Si–5Cr shape memory alloy

A. Syed Bava Bakrudeen [1], D. Jeyasimman [1,*], A. Balaji [2]

[1]*Department of Mechanical Engineering, Periyar Maniammai Institute of Science and Technology, Vallam, India*
[2]*Department of Mechanical Engineering, Al Ameen Engineering College, Erode, India*

ARTICLE INFO

Article history:
Received 18 January 2022
Received in revised form
12 April 2022
Accepted 31 May 2022

Keywords:
Shape memory alloy
Shape memory effect
Mechanical alloying

ABSTRACT

Mechanical alloying and consequent sintering techniques were used to create a bulk alloy of Fe–28Mn–6Si–5Cr from elemental powder. The microstructure and shape memory behavior due to bending deformation were investigated. The majority of α phases that existed at the start of the mechanical alloying process were changed into γ phases by the end of the 40-hour process. The γ phase was essential to achieving shape recovery behavior, which was boosted by mechanical alloying. A stress-induced γ to ε phase transformation occurred at the end of the bending deformation process. Shape recovery was observed after the subsequent heat treatment process due to reverse martensitic ε to γ phase transformation. After mechanical alloying, a grain size of 9.5 nm was attained and a considerable amount of shape recovery was achieved at the end of the recovery heat-treatment process. As a result, we came to the conclusion that combining mechanical alloying with powder metallurgy and then sintering has the potential to synthesize Fe-Mn-Si-Cr shape memory alloy.

1. Introduction

For the synthesis of shape memory alloys (SMAs) and MMCs, high-energy ball milling is a strong approach. Mechanical alloying (MA) is one of the most common ways to make nano-crystalline materials. MA is a process that involves repeated deformation, cold-welding, and fracture. BPR (Ball to Powder ratio), speed, milling atmosphere, temperature, temperature process control agent, particle size, volume fraction, and types of alloy materials are important parameters that influence the stages of milling (Suryanarayana, 2001). Otsuka et al. (1990) investigated Fe-Mn-Si SMA by adding a different alloying element like Mn, Cr, Ni and produced 16 different combinations of SMA and ascertained the recovery strain, martensite start (Ms), austenite (As), and Neel temperature (TN), and they concluded that the addition of alloying element and thermomechanical treatment improved the SME of Fe-Mn-Si SMA (Otsuka et al., 1990).

Li et al. (2008) carried out a texture evolution analysis of warm rolled Fe–28Mn–6Si–5Cr SMA, and concluded γ fiber component develops, which is attributed to the alignment of twin-matrix lamellas, and a noticeable texture transition takes place between 44 and 57% rolling reduction at 873K due to gross orientation being the dominant texture component. Dogan and Arslan (2012) experimentally studied phase transitions associated with Fe–20Mn–6Si–9Cr during mechanical alloying and then successive annealing. Dogan and Arslan (2012) concluded the optimum-milling time at 300 rev/min was 20 h, during which a new phase called the martensite phase, formed at 1323K for 30 min. The formation of this phase strictly depends on milling time. A solid solution was formed after more than 0 h of milling. After 20 h of milling, the alloy's particle size had shrunk by 0.1μm (Dogan and Arslan, 2012). Jeyasimman et al. (2014a) successfully produced a bulk nanocrystalline Al6061 matrix reinforced with different weight percentages of TiC nanoparticles by MA. TEM confirmed that these TiC were uniform nanoparticles distributed among the given Al6061 matrix. Al6061-2.0% TiC nanocomposites achieved a crystallite size of approximately 68 nm. The relative density of Al6061-0.5% TiC nanocomposite was decreased due to the domination of work hardening and increased due to the domination of the reduction in the powder (Jeyasimman et al., 2014a). In comparison to coarse

* Corresponding Author.
Email Address: jeyasimman76@gmail.com (D. Jeyasimman)
https://doi.org/10.21833/ijaas.2022.09.005
Corresponding author's ORCID profile:
https://orcid.org/0000-0002-0780-9609

grain size, Kim et al. (2018) created an ultra-fine grained Fe-Mn-Si shape memory alloy with excellent strength and greatly improved shape recovery stress. They used differential speed rolling with speed ratios ranging from 2 to 3.8 in their experiment (Kim et al., 2018). A Fe-28Mn-6Si-5Cr (Mass %) shape memory alloy was used as a self-adjustable axial preloading of ball bearings (Paleu et al., 2018). An experimental investigation on the rate dependency of thermomechanical and stress-induced martensitic transformation behavior in Fe-28Mn-6Si-5Cr shape memory alloy under compression was studied by Cao and Iwamoto (2019). They revealed that the volume fraction of stress-induced ε-martensite under compression becomes smaller than that under tension. In the unloading process of compression, a higher strain rate dependency of temperature change was obtained. Finally, by changing the compressive strain rate under quasi-static level, the ratio of shape recovery can be improved to 7.14 % due to the opposite rate dependency of the ratio of shape recovery can be obtained under tensile and compressive stress (Cao and Iwamoto, 2019).

The present study and investigation are focused on the synthesis, characterization, and structural development of the Fe-Mn-Si-Cr shape memory alloy powder by MA. TEM-SAD, XRD, and SEM-EDS techniques were used to examine the effects of different milling times on this alloy. The powder was compressed and sintered after milling, and shaper recovery due to bending deformation was investigated.

2. Materials and methods

A major alloy metal used for fabrication was pure iron (Fe) metal powder with a purity of more than 99.5% and a mesh size of -200. The remaining metal powders were manganese (Mn) (purity of 99%) and mesh size of -325, silicon with a purity of 98.5%, and mesh size of -200 chromium with less than 1% impurity at the -100 mesh size (Xu et al., 2016a). SISCO Laboratories Pvt. Limited, Navi-Mumbai, India, supplied the raw materials.

The single jar high-energy planetary mill was filled with 61 wt.% Fe, 28 wt.% Mn, 6 wt.% Si, and 5 wt.% Cr. The materials were milled in a highly pure wet agent (Toluene) to avoid the formation of intermetallic compounds during milling. Thirty highly hardened 10-mm diameter Titanium Carbide (TiC) balls, each weighing 10 g, were sealed with 100g of Fe-28Mn-6Si-5Cr powder mixture in a TiC vial. The ball to powder (BPR) ratio was set at 3:1. The corresponding bowl vial speed was 250 rpm. The total MA processing time was set at 40 h. However, every 5 h, the powder samples were collected for characterization studies (Xu et al., 2015).

The square mold used to compact the specimen has 20 mm sides and a 25 mm height; we created 20 mm-sided and 15 mm-high specimens with this mold. A double-action compacting machine made by VB Ceramics Pvt. Ltd, Chennai, India with a maximum capacity of 20 tonnes was used to apply 750 MPa pressure on both sides of the specimen (Xu et al., 2016b).

The compacted specimen was sintered in a tubular furnace built in a controlled atmosphere with argon purging. A furnace with a maximum heating capacity of 1600°C was used. The specimens were heated at a temperature of 1200°C for around 4 h with Argon gas shielding (Xu et al., 2017).

The SME of the bulk alloy was examined by bending tests after 2%, 4%, and 6% bending deformation and subsequent recovery heat treatment at 400°C for 15 minutes with a controlled argon atmosphere as a shielding medium, using a 15 mm gauge length specimen. A Universal Testing Machine with a maximum capacity of 50 KN and a strain rate of 6.3 x 10-4 was used to perform the bending test. The shape recovery was evaluated using Eq. 1.

$$Shape\ recovery\ (\%) = \frac{(180-\theta_e-\theta_r)}{(180-\theta_e)} \times 100 \quad (1)$$

The amount of prestrain was estimated using formulae $\varepsilon = t/d$ and implemented by the appropriate mandrel diameter (d) (Maji et al., 2011). The 20 mm square samples were cut into 0.5 mm thick pieces using wire cut EDM.

3. Result and discussion

3.1. Powder alloy characterization

The X-Ray Diffraction (XRD) patterns recorded for the Fe–28Mn–6Si–5Cr powder mixtures with different milling times were examined to analyze the features of the phase formation of MA (Liu and Chen, 2018). It contains diffraction peaks at the α–Fe and Cr (B.C.C crystal structure), Mn (B.C.C crystal structure), and Si (Diamond Cubic F.C.C). After 5 h of mechanical milling, Cr was fully dissolved in α–Fe. The XRD pattern of the mixture prepared to use MA with a minimum exposure time shows peak broadening, indicating that grains were refined and disintegrated into subgrains (Liu and Chen, 2018). The small shift in peaks at the α–Fe phase towards greater 2θ angles and the significant reduction in the intensity of the peaks at Mn demonstrated that Mn was dissolved in the α–Fe. The reason for this is that the percentage of the dissolved components was small during the initial stage of MA and because of the insignificant difference between the atomic radii of Fe, Cr, Mn, and Si (Druker et al., 2018). After 40 h of MA, Mn was completely dissolved in the α–Fe phase and the dissolution of Si in α–Fe was more intense. In the XRD patterns of these powder mixtures, the peaks at Si shifted towards smaller 2θ angles, demonstrating that the lattice parameter of this phase increased and Si was dissolved in this phase. After MA for 40 hrs, only the Fe phase remains in the powder mixture. Since the

composition of the equilibrium state is two-phase, it can be inferred that this phase was a supersaturated solid solution (Druker et al., 2018; Kong et al., 2018). The α-Fe is completely phase-shifted to γ-Fe due to mechanical alloying.

The structural characteristics of the alloy Fe-28Mn-6Si-5Cr are given in Table 1. Crystalline size and lattice strain concerning milling time were calculated. The pseudo-Voigt function was used to measure peak shaping. It is a combination of Lorentzian and Gaussian functions. According to our calculation, the crystalline size has decreased from 35.2 nm to 9.5 nm. Fig. 1a shows that matrix crystallite size decreases as a function of increasing milling time. However, lattice strains were increased due to severe plastic deformation (SPD) and fracture of powder particles in high-energy ball mills as well as increased milling time (Sivasankaran et al., 2010). It has been known that successful mechanical alloying depends on a critical balance between cold welding and fracturing, which enables powder particles to always be in contact with each other on atomically clean surfaces, minimizing diffusion distance (Xu et al., 2016a). At the stage of 20 hrs of milling, the agglomerated particle size starts to decrease (Fig. 1b), suggesting the fracturing process is beginning to become more dominant over the agglomeration process with increasing milling time, probably owing to solid solution hardening by mechanical alloying as well as dispersion hardening of the composite powder with milling time (Jeyasimman et al., 2014a). After milling for another 30 hours (Fig. 1c), the particle size decreased further and the particle size distribution appeared more uniform in size. Finally, a steady-state was reached (Fig. 1d) during further milling. After 30 h of MA, almost equiaxed powder particles were obtained. Thus, milling was carried out for up to 40 h (Nespoli et al., 2019; Velmurugan et al., 2018).

Table 1: Structural parameters of Fe-28Mn-6Si-5Cr powder alloy with different milling time

Milling Time in h	Crystallite size in nm	Lattice Strain in %
5	35.2	0.4381
10	32.4	0.8734
15	25.8	0.9918
20	24.5	1.2942
25	23.8	1.4071
30	18.3	2.1358
35	15.2	2.3592
40	9.2	2.8561

The EDS analysis of the Fe–28Mn–6Si–5Cr alloy powder (Fig. 2) ensured that the MA did not introduce any contamination into the milled powder. Fig. 2 shows Fe, Mn, Cr, and Si peaks were the only ones visible in the spectrum. The clear peaks indicating the presence of any other elements were not heavily contaminated (Lü and Lai, 1997; Jeyasimman et al., 2015). A small amount of carbon and oxygen are negligible amounts of impurities, and the present very small amount of gold (Au) and actinium (Ac) is not contaminated, it is a raw material used for the EDS test.

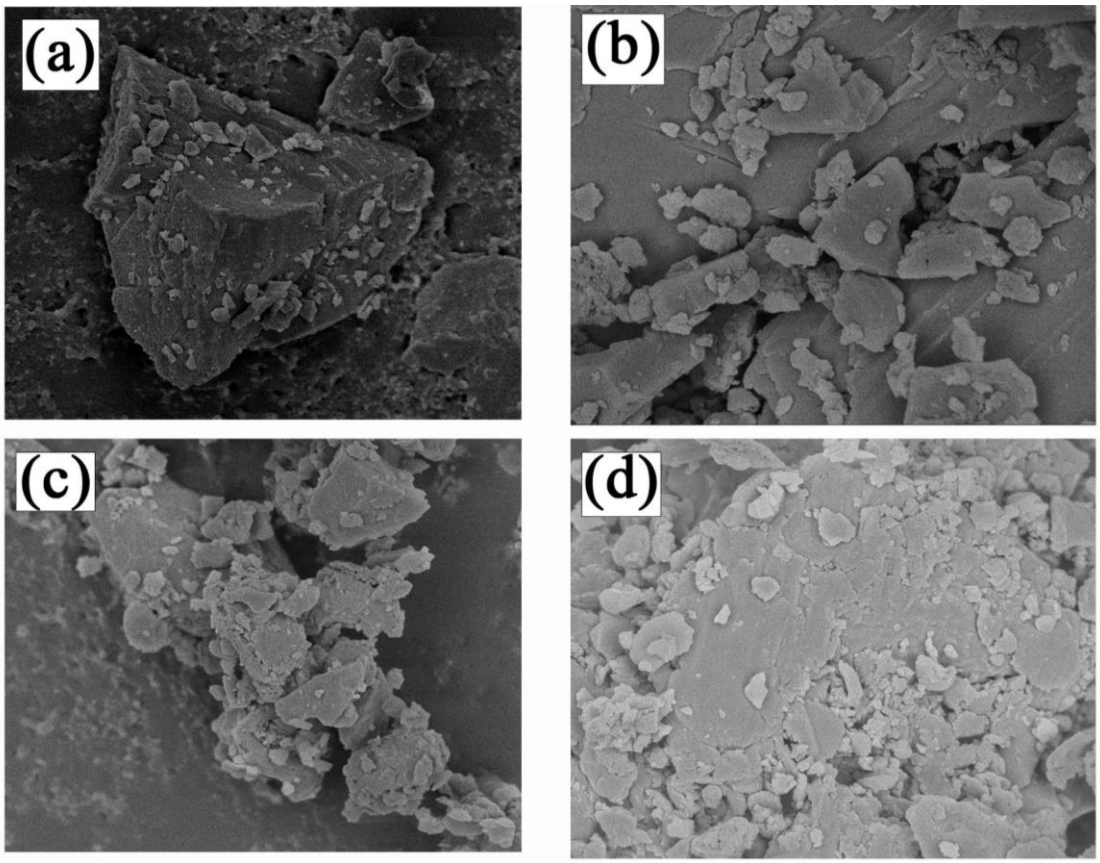

Fig. 1: FESEM morphology of Fe–28Mn–6Si–5Cr alloy powder as a function of the milling time after: (a) 5 h; (b) 20 h; (c) 30 h; (d) 40 h

Fig. 3 shows a TEM image of a typical Fe–28Mn–6Si–5Cr powder alloy after 5 h and 40 h. It was not easy to discover the crystallite grain size directly from the dazzling field of the TEM image (Kursun and Gogebakan, 2015). In Fig. 4a, the SAED pattern diffuse ring is shown on the inner side of the pattern with very few bright spots on the outer side, so after 5 h of milling, the Fe–28Mn–6Si–5Cr alloy powder is in the amorphous stage with a small amount of single crystalline form. The diffraction ring related to Mn and α-Fe were detected in Figs. 4b-4c. It reveals that powder is made of many nano-crystalline elements like Mn, Si, and Cr that are distributed in the matrix of α-Fe, which is in amorphous form.

Fig. 5a. shows that a small spot made up of rings reveals that the alloy has changed to the polycrystalline stage. The particle size of SMA powder after 40 h of milling is 9.5 nm. Hence, at this stage, SMA powder changed from an amorphous to a polycrystalline form. Each spot arising from Bragg's reflection of an individual crystallite reveals that the powder is made of polynanocrystalline of uniform contrast, which was acquired from Mn, Si, and Cr powders that are uniformly distributed and evenly dispersed in α-Fe powder (Liu et al., 2019).

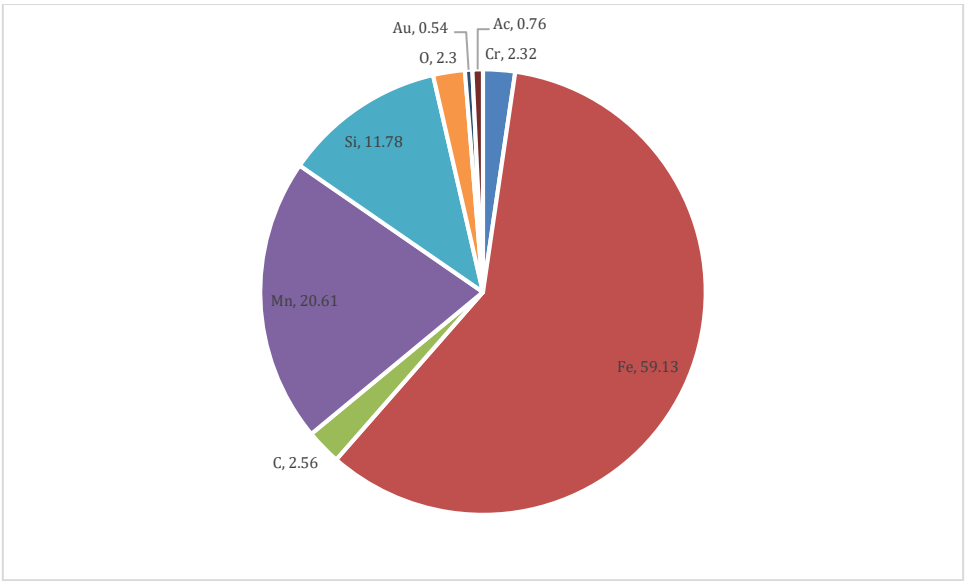

a

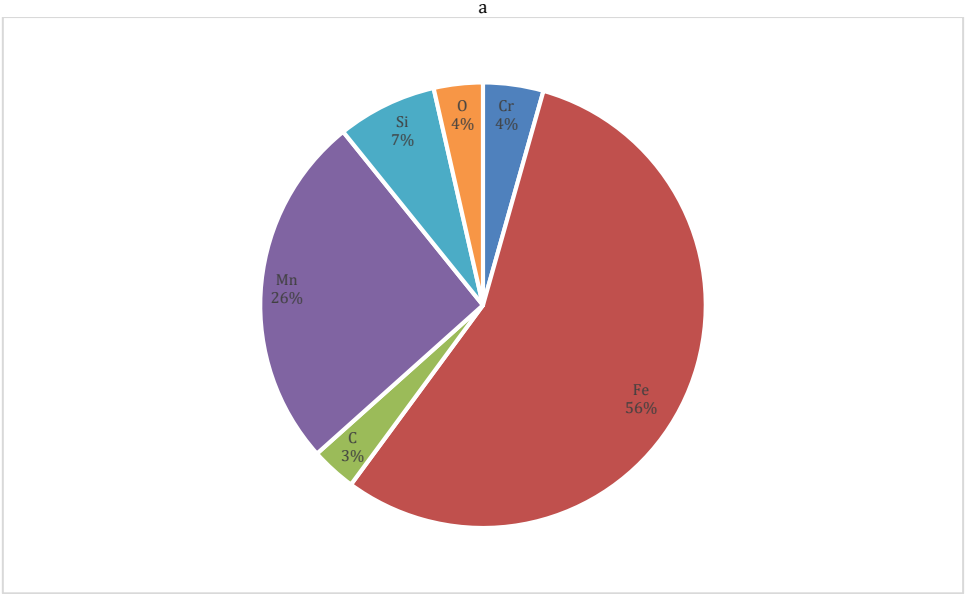

b

Fig. 2: EDS images of Fe–28Mn–6Si–5Cr alloy powder as a function of the milling time after (a) 5 h; (b) 40 h

3.2. Shape recovery of bulk alloy

A schismatic diagram of shape recovery versus pre-strain of Fe–28Mn–6Si–5Cr bulk alloy was shown in Fig. 6. The percentage of shape recovery decreases with an increase in the percentage of prestrain shown in Table 2. The highest amount of shape recovery is achieved at 2% of prestrain. The FCC γ austenite formed after sintering of the bulk alloy is shown in Fig. 7a.

Table 2: Shape recovery of Fe–28Mn–6Si–5Cr bulk alloy versus applied pre-strain due to bending deformation

Pre-strain in %	2	4	6
Recovery in %	8.2	5.5	1

This partial γ iron changed into HCP ε iron due to prestrain shown in Fig. 7b. When prestrained alloy HCP ε iron was subjected to recovery heat treatment, it partially recovered to FCC γ austenite and partially changed into BCC ά martensite. BCC ά martensite was formed as a result of the Shockley partial dislocation of γ-ε-ά reverse transformation. This ά-martensite acts as a barrier toward reverse shape recovery formation (Maji et al., 2011). In between these transformations, intermetallics are formed as shown in Fig. 7c (Bakrudeen et al., 2022).

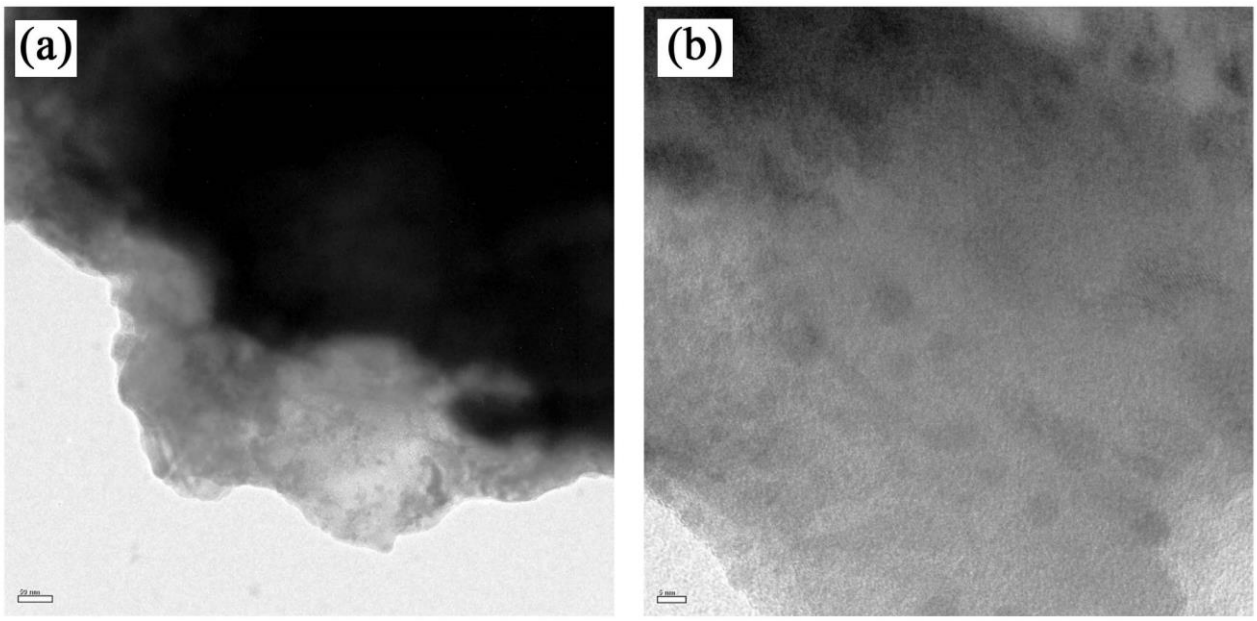

Fig. 3: TEM images of Fe–28Mn–6Si–5Cr alloy powder as a function of the milling time after (a) 5 h; (b) 40 h

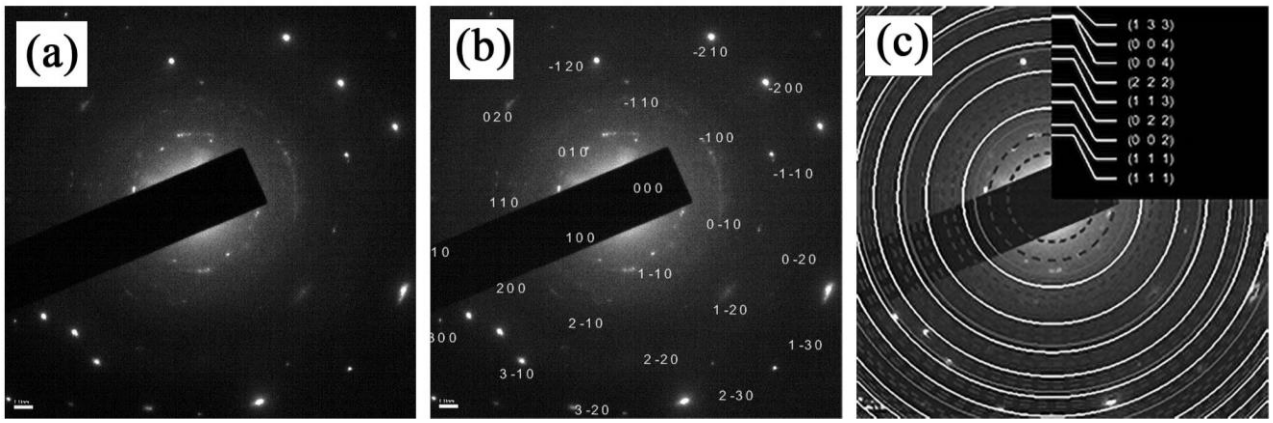

Fig. 4: The SAD pattern of alloy powder after 5 h milling

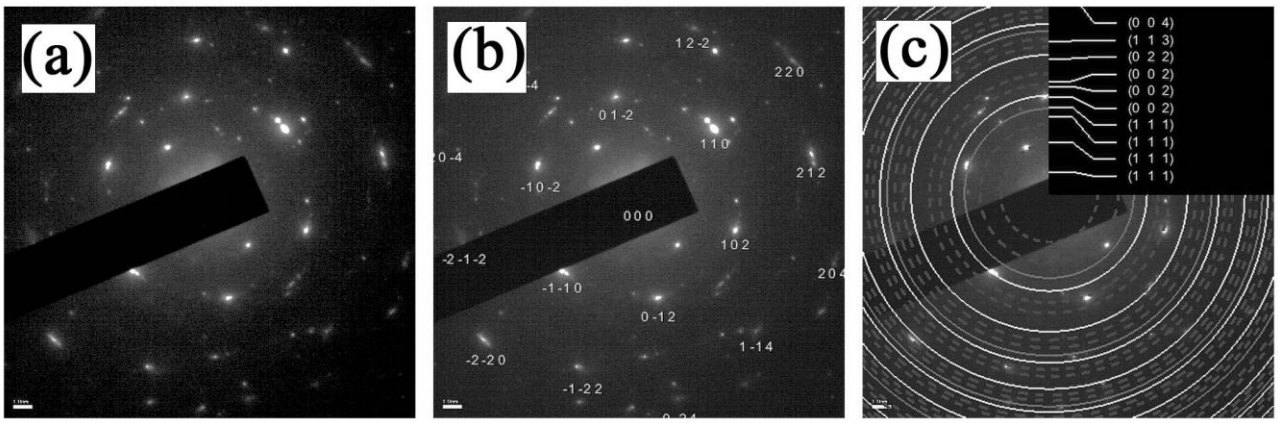

Fig. 5: The SAD pattern of alloy powder after 40 h milling

Fig. 8 demonstrates that the EDS results of sintered Fe-28Mn-6Si-5Cr SMA were 91.67 wt.% contamination-free; a minor 8.33 wt.% of oxygen was unavoidable due to the rapidly oxidized nature of alloying components such as Fe, Mn, Si, and Cr. According to our reference research (Jeyasimman et

al., 2014b), the oxidations are within our specified limit.

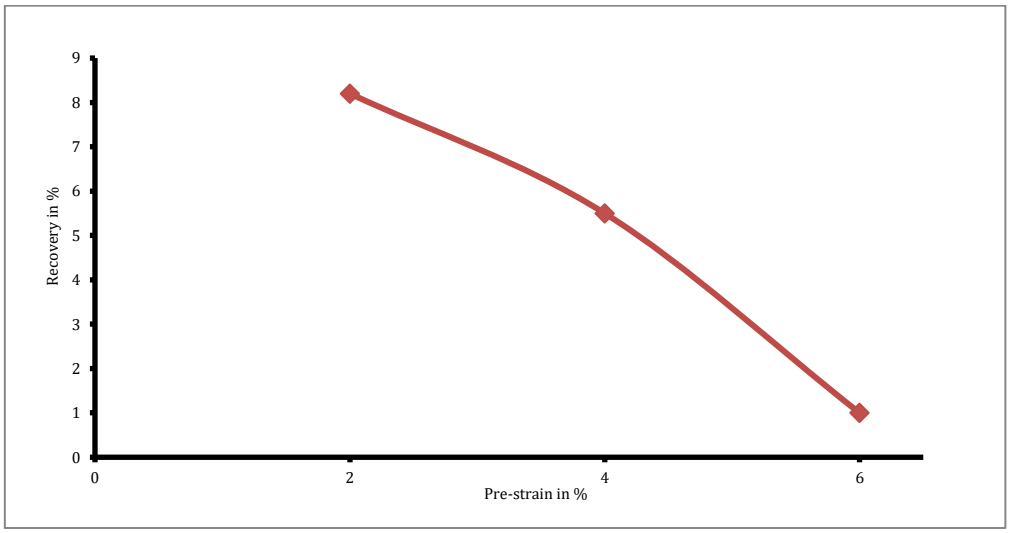

Fig. 6: Shape recovery due to heat treatment

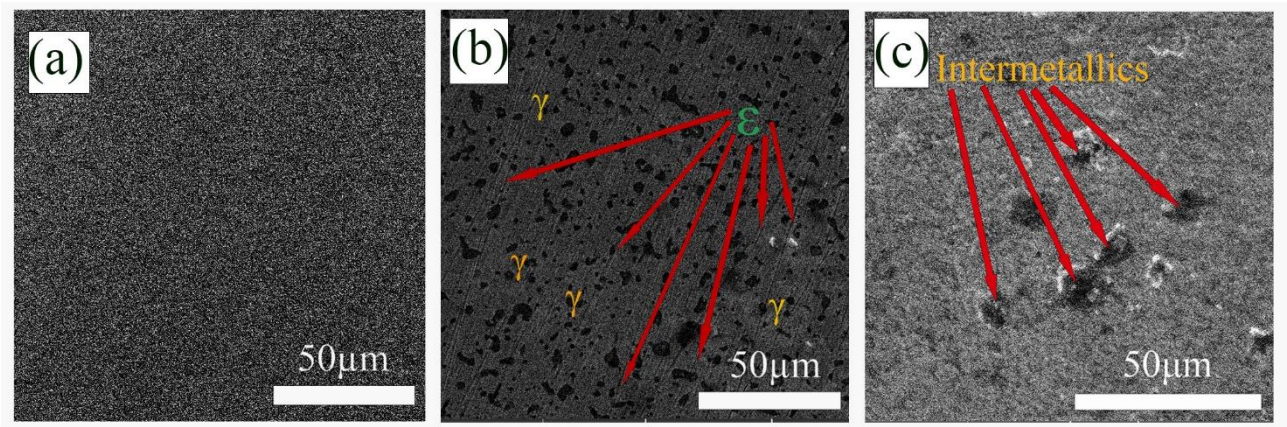

Fig. 7: SEM images of sintered Fe–28Mn–6Si–5Cr bulk alloy (a) After sintering (b) after 4% deformation (c) After recovery heat treatment

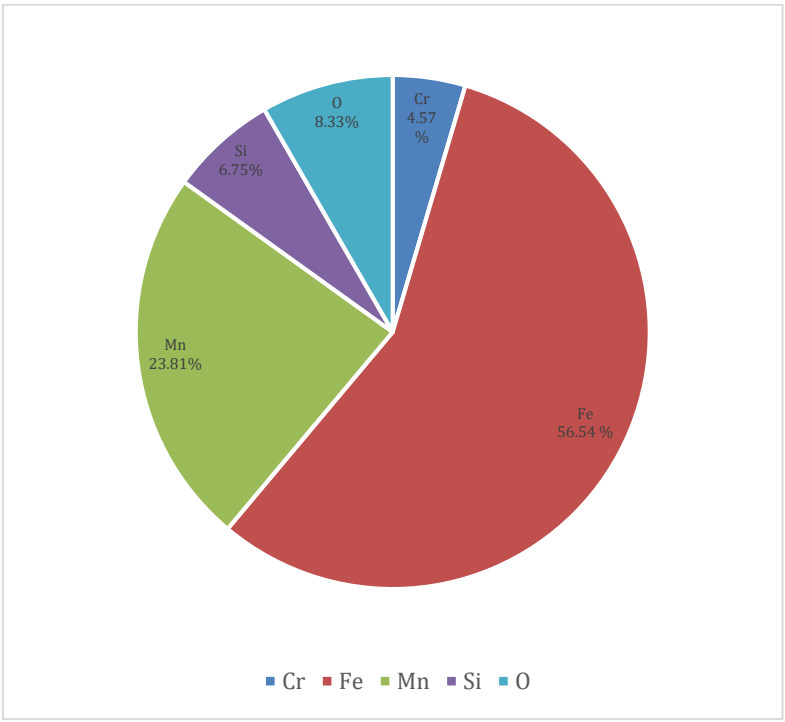

Fig. 8: EDS result of sintered of Fe–28Mn–6Si–5Cr alloy

4. Conclusion

The microstructural evolution of Fe-Mn-Si-Cr powder during different MA was clarified, and the following results were obtained:

1. The Fe-Mn-Si-Cr shape memory alloy powders were fabricated by high-energy ball milling. After 40 h of milling, the crystallite size was around 9.5 nm due to a high fracturing tendency. A uniform distribution of alloy powder was successfully achieved, as evidenced by SEM and TEM micrographs. The EDS results show that the powder alloy was not contaminated.
2. Shape recovery due to bending deformation was examined and achieved a desirable result. We achieved a higher percentage of shape recovery at 2% of prestrain.
3. Both the powder and the bulk alloy were not contaminated, which had been proven in EDS studies.

Compliance with ethical standards

Conflict of interest

The author(s) declared no potential conflicts of interest with respect to the research, authorship, and/or publication of this article.

References

Bakrudeen ASB, Jeyasimman D, and Balaji A (2022). Effect of compaction pressure, sintering temperature and recovery heat treatment temperature of powder metallurgical Fe-20Mn-5Si-5Ni-8Cr shape memory alloy. MRS Advances, 7(10): 222-228. https://doi.org/10.1557/s43580-022-00247-w

Cao B and Iwamoto T (2019). An experimental investigation on rate dependency of thermomechanical and stress-induced martensitic transformation behavior in Fe-28Mn-6Si-5Cr shape memory alloy under compression. International Journal of Impact Engineering, 132: 103284. https://doi.org/10.1016/j.ijimpeng.2019.04.026

Dogan A and Arslan H (2012). Effect of ball-milling conditions on microstructure during production of Fe–20Mn–6Si–9Cr shape memory alloy powders by mechanical alloying. Journal of Thermal Analysis and Calorimetry, 109(2): 933-938. https://doi.org/10.1007/s10973-011-1809-x

Druker A, Vermaut P, and Malarría J (2018). The shape recovery conditions for Fe–Mn–Si alloys: an interplay between martensitic transformation and plasticity. Materials Characterization, 139: 319-327. https://doi.org/10.1016/j.matchar.2018.03.018

Jeyasimman D, Narayanasamy R, and Ponalagusamy R (2015). Role of hybrid reinforcement on microstructural observation, characterization and consolidation behavior of AA 6061 nanocomposite. Advanced Powder Technology, 26(4): 1171-1182. https://doi.org/10.1016/j.apt.2015.05.013

Jeyasimman D, Sivaprasad K, Sivasankaran S, and Narayanasamy R (2014b). Fabrication and consolidation behavior of Al 6061 nanocomposite powders reinforced by multi-walled carbon nanotubes. Powder Technology, 258: 189-197. https://doi.org/10.1016/j.powtec.2014.03.039

Jeyasimman D, Sivasankaran S, Sivaprasad K, Narayanasamy R, and Kambali RS (2014a). An investigation of the synthesis, consolidation and mechanical behaviour of Al 6061 nanocomposites reinforced by TiC via mechanical alloying. Materials and Design, 57: 394-404. https://doi.org/10.1016/j.matdes.2013.12.067

Kim YS, Choi E, and Kim WJ (2018). Characterization of the microstructures and the shape memory properties of the Fe-Mn-Si-Cr-Ni-C shape memory alloy after severe plastic deformation by differential speed rolling and subsequent annealing. Materials Characterization, 136: 12-19. https://doi.org/10.1016/j.matchar.2017.11.055

Kong J, Song X, Shao X, Liu X, and Feng S (2018). The preparation, formation mechanism and magnetic properties of a Fe-Cr-Mn-N amorphous alloy. Advanced Powder Technology, 29(12): 3348-3356. https://doi.org/10.1016/j.apt.2018.09.013

Kursun C and Gogebakan M (2015). Characterization of nanostructured Mg–Cu–Ni powders prepared by mechanical alloying. Journal of Alloys and Compounds, 619: 138-144. https://doi.org/10.1016/j.jallcom.2014.08.126

Li H, Yin F, Sawaguchi T, Ogawa K, Zhao X, and Tsuzaki K (2008). Texture evolution analysis of warm-rolled Fe–28Mn–6Si–5Cr shape memory alloy. Materials Science and Engineering: A, 494(1-2): 217-226. https://doi.org/10.1016/j.msea.2008.05.013

Liu J and Chen W (2018). Microstructure and mechanical properties of a spark plasma sintered Fe-11Cr-2.3 B-6Al-15Mn alloy. Vacuum, 150: 49-57. https://doi.org/10.1016/j.vacuum.2018.01.029

Liu X, Cheng H, Li Z, Wang H, Chang F, Wang W, and Dai P (2019). Microstructure and mechanical properties of FeCoCrNiMnTi0. 1C0. 1 high-entropy alloy produced by mechanical alloying and vacuum hot pressing sintering. Vacuum, 165: 297-304. https://doi.org/10.1016/j.vacuum.2019.04.043

Lü L and Lai MO (1997). Mechanical alloying. Springer Science and Business Media, Berlin, Germany.

Maji BC, Krishnan M, and Ray RK (2011). Role of Si in improving the shape recovery of FeMnSiCrNi shape memory alloys. Metallurgical and Materials Transactions A, 42(8): 2153-2165. https://doi.org/10.1007/s11661-011-0651-x

Nespoli A, Villa E, and Passaretti F (2019). Effect of annealing on the microstructure of Yttrium-doped NiTiCu shape memory alloys. Journal of Alloys and Compounds, 779: 30-40. https://doi.org/10.1016/j.jallcom.2018.11.228

Otsuka H, Yamada H, Maruyama T, Tanahashi H, Matsuda S, and Murakami M (1990). Effects of alloying additions on Fe-Mn-Si shape memory alloys. The Iron and Steel Institute of Japan (ISIJ) International, 30(8): 674-679. https://doi.org/10.2355/isijinternational.30.674

Paleu V, Gurău G, Comăneci RI, Sampath V, Gurău C, and Bujoreanu LG (2018). A new application of Fe-28Mn-6Si-5Cr (mass%) shape memory alloy, for self-adjustable axial preloading of ball bearings. Smart Materials and Structures, 27(7): 075026. https://doi.org/10.1088/1361-665X/aac4c5

Sivasankaran S, Sivaprasad K, Narayanasamy R, and Iyer VK (2010). An investigation on flowability and compressibility of AA 6061100−x-x wt.% TiO2 micro and nanocomposite powder prepared by blending and mechanical alloying. Powder Technology, 201(1): 70-82. https://doi.org/10.1016/j.powtec.2010.03.013

Suryanarayana C (2001). Mechanical alloying and milling. Progress in Materials Science, 46(1-2): 1-184. https://doi.org/10.1016/S0079-6425(99)00010-9

Velmurugan C, Senthilkumar V, Biswas K, and Yadav S (2018). Densification and microstructural evolution of spark plasma sintered NiTi shape memory alloy. Advanced Powder Technology, 29(10): 2456-2462. https://doi.org/10.1016/j.apt.2018.06.026

Xu Z, Hodgson MA, and Cao P (2015). A comparative study of powder metallurgical (PM) and wrought Fe–Mn–Si alloys. Materials Science and Engineering: A, 630: 116-124. https://doi.org/10.1016/j.msea.2015.02.021

Xu Z, Hodgson MA, and Cao P (2016a). Effect of immersion in simulated body fluid on the mechanical properties and biocompatibility of sintered Fe–Mn-based alloys. Metals, 6(12): 309. https://doi.org/10.3390/met6120309

Xu Z, Hodgson MA, and Cao P (2016b). Effects of mechanical milling and sintering temperature on the densification, microstructure and tensile properties of the Fe–Mn–Si powder compacts. Journal of Materials Science and Technology, 32(11): 1161-1170. https://doi.org/10.1016/j.jmst.2016.08.024

Xu Z, Hodgson MA, Chang K, Chen G, Yuan X, and Cao P (2017). Effect of sintering time on the densification, microstructure, weight loss and tensile properties of a powder metallurgical Fe-Mn-Si alloy. Metals, 7(3): 81. https://doi.org/10.3390/met7030081